Comparison of zero-sequence injection methods in cascaded H-bridge multilevel converters for large-scale photovoltaic integration

Yu, Yifan; Konstantinou, Georgios; Townsend, Christopher David; Agelidis, Vassilios

Published in:
I E T Renewable Power Generation

Link to article, DOI:
10.1049/iet-rpg.2016.0621

Publication date:
2017

Document Version
Peer reviewed version

Comparison of Zero-Sequence Injection Methods in Cascaded H-Bridge Multilevel Converters for Large-Scale Photovoltaic Integration

Yifan Yu[1], Georgios Konstantinou[1,*], Christopher D. Townsend[2], Vassilios G. Agelidis[3]

[1]School of Electrical Engineering and Telecommunications, UNSW Australia, Sydney, NSW, 2052, Australia
[2]School of Electrical Engineering and Computer Science, University of Newcastle, Newcastle, Australia
[3]Department of Electrical Engineering, Technical University of Denmark, Copenhagen, Denmark
[*]g.konstantinou@unsw.edu.au

Abstract: Photovoltaic (PV) power generation levels in the three phases of a multilevel Cascaded H-Bridge (CHB) converter can be significantly unbalanced, owing to different irradiance levels and ambient temperatures over a large-scale solar PV power plant. Injection of a zero-sequence voltage is required to maintain three-phase balanced grid currents with unbalanced power generation. This paper theoretically compares power balance capabilities of various zero-sequence injection methods based on two metrics which can be easily generalized for all CHB applications to PV systems. Experimental results based on a 430 V, 10 kW, three-phase, seven-level cascaded H-bridge converter prototype confirm superior performance of the Optimal Zero-Sequence Injection technique.

1. Introduction

Multilevel converters are being investigated as next-generation power converters for large-scale photovoltaic (PV) power plants, owing to their high conversion efficiency and modular structure [1–27]. Among them, the Cascaded H-Bridge (CHB) multilevel converter, in particular, is considered as one of the most suitable options, due to the presence of multiple independent dc links and the ability to extend to higher levels [4–27]. Fig. 1 shows the typical layout of a star-connected, three-phase, $(2N+1)$-level CHB converter, which consists of $3N$ H-bridges, each fed by multiple PV strings via separate dc-dc converters.

The dc-side capacitor voltage v_{dc} is regulated via Voltage Oriented Control (VOC) [20, 21], while each dc-dc converter conducts independent Maximum Power Point Tracking (MPPT) [10] to maximize the power extracted from the PV strings. The modular structure allows easy extension to reach higher voltage and power levels, thus making it feasible to connect a large-scale PV farm to a medium voltage network with a single converter. A high-frequency transformer in the dc-dc stage can limit the voltage to which PV modules are subjected. Bulky and heavy line-frequency power transformers are no longer necessary, since galvanic isolation has already been provided by compact high-frequency transformers.

A unique characteristic of CHB converters in PV applications, due to the converter being formed from multiple single-phase legs, is that there can be significant differences in the power generated

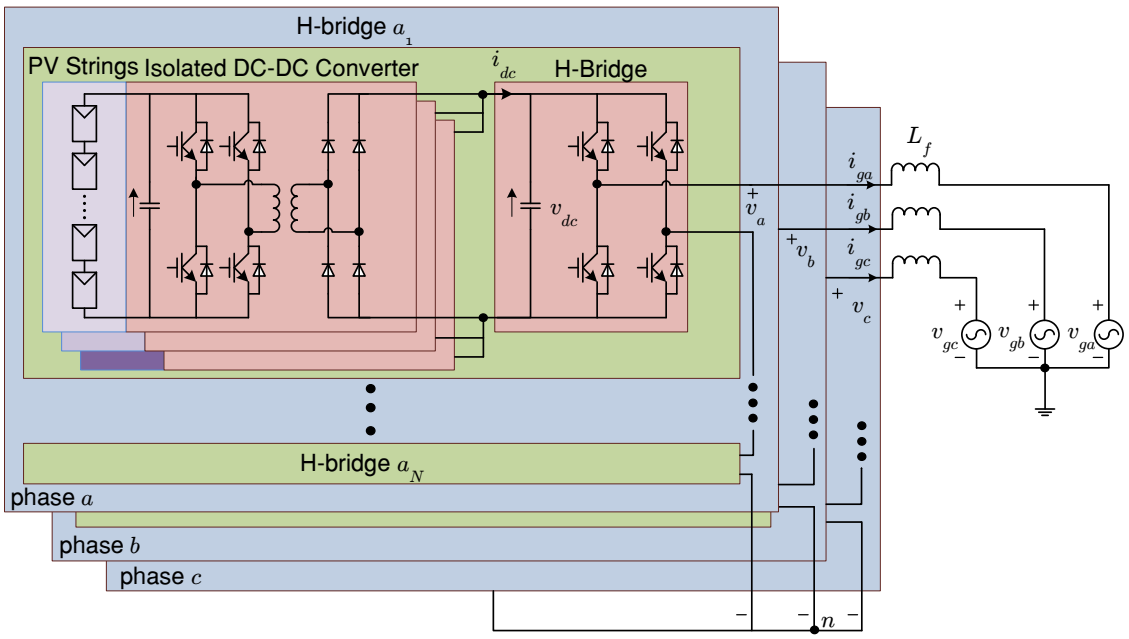

Fig. 1. *Star-connected, three-phase, $(2N+1)$-level cascaded H-bridge converter.*

by the PV modules connected to each bridge, because of non-uniform solar irradiance, unequal ambient temperatures, partial shading and/or inconsistent module degradation. This power imbalance problem can be classified into two categories [21]: (a) *inter-phase power imbalance*, which occurs when each phase generates different amounts of power; and (b) *inter-bridge power imbalance*, which occurs when bridges in the same phase leg generate different amounts of power.

One way to solve the inter-phase power imbalance of star-connected three-phase CHB converters is to inject a zero-sequence component into the converter output voltages. Various zero-sequence injection methods have been developed so far [20–24]. A Fundamental Frequency Zero-Sequence Injection (FFZSI) method was derived through instantaneous power theory [20] and phasor diagrams [21], respectively. A Weighted Min-Max (WMM) zero-sequence injection method was derived in [22] and implemented in [23]. Furthermore, three methods, namely, Double 1/6 Third Harmonic Injection (DTHI), Reduced Third Harmonic Injection (RTHI), and Double Min-Max (DMM) zero-sequence injection, were also proposed in [21]. In addition, the Optimal Zero-Sequence Injection (OZSI) and Simplified Optimal Zero-Sequence Injection (SOZSI), were presented in [24].

The power balance capabilities of these zero-sequence injection methods have been theoretically compared (without experimental confirmation) in [25] with both qualitative and quantitative metrics. The qualitative metric (Energy-Balancing Diagram) is only a two-dimensional representation of viable imbalance cases which can be rebalanced with zero-sequence injection methods, and the quantitative metric (Total Covered Area) does not directly reflect the percentage of viable cases among all possible power imbalance cases.

This paper provides both theoretical and experimental evaluation and comparison of the zero-sequence injection methods. The preliminary concepts of power balance space and power balance factor in [26,27] are extended, so that metrics are only dependent on the voltage overrating, regardless of the application-specific details of converter, grid and PV arrays. The power balance factor directly reflects the percentage of viable cases that can be rebalanced among all possible power

imbalance cases. The final results provide a conclusive evaluation of the methods that has general function and application. This paper also demonstrates that the WMM method [22,23] synthesizes an incorrect fundamental frequency zero-sequence component, which leads to the reduction in system dynamic performance. Experimental results based on a 430 V, 10 kW, three-phase, seven-level cascaded H-bridge converter prototype are provided to confirm the superior performance of OZSI amongst all zero-sequence injection methods.

2. Review of Zero-Sequence Injection Methods

The three-phase power generation ratios, reflecting the actual power generation level in each phase, are defined as [21]:

$$\lambda_{a,b,c} = \frac{p_{a,b,c}}{P_{nom}/3}, \tag{1}$$

where the average power generation ratio $\bar{\lambda}$:

$$\bar{\lambda} = \frac{\lambda_a + \lambda_b + \lambda_c}{3}. \tag{2}$$

When the three-phase power generation levels are unequal, injection of a zero-sequence into the converter output voltages is necessary [20–24]:

$$v_a = v_a^+ + v^0, \tag{3a}$$
$$v_b = v_b^+ + v^0, \tag{3b}$$
$$v_c = v_c^+ + v^0, \tag{3c}$$

where v_a^+, v_b^+, v_c^+ represent the positive-sequence components.

2.1. Fundamental Frequency Zero-Sequence Injection (FFZSI)

The injection of a fundamental frequency zero-sequence component into the converter output voltages is able to rebalance the three-phase grid currents, when the three-phase power generation levels are unequal [20, 21]. The injected zero-sequence vector $\mathbf{V^0}$ redistributes power among the three phases with the grid current vectors $\mathbf{I_{ga}}$, $\mathbf{I_{gb}}$, $\mathbf{I_{gc}}$, as shown in Fig. 2. FFZSI can be derived as [21]:

$$v_{FF}^0 = \sqrt{2}V^0 \cos(\omega t + \theta), \tag{4}$$

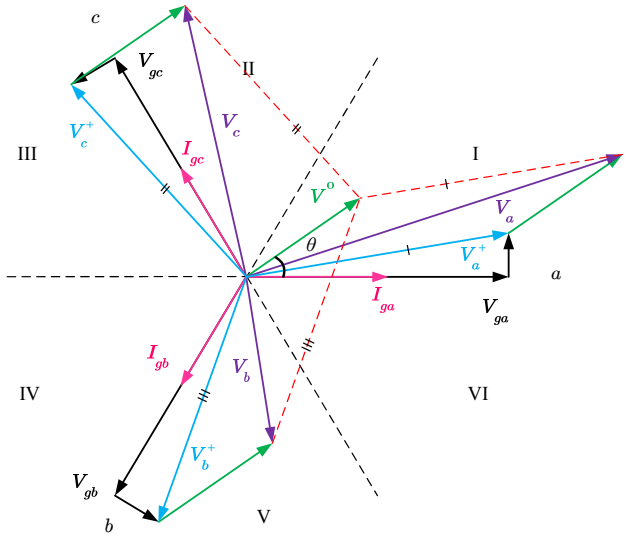

Fig. 2. *Phasor diagram with FFZSI.*

where:

$$V^0 = \frac{\sqrt{6}\Delta}{3(\lambda_a + \lambda_b + \lambda_c)} V_g, \tag{5a}$$

$$\theta = \begin{cases} \sin^{-1}\left(\dfrac{\sqrt{6}\,(\lambda_c - \lambda_b)}{2\Delta}\right) & \text{Sectors (I), (VI)} \\ \dfrac{2\pi}{3} + \sin^{-1}\left(\dfrac{\sqrt{6}\,(\lambda_b - \lambda_a)}{2\Delta}\right) & \text{Sectors (II), (III)} \\ \dfrac{4\pi}{3} + \sin^{-1}\left(\dfrac{\sqrt{6}\,(\lambda_a - \lambda_c)}{2\Delta}\right) & \text{Sectors (IV), (V)} \end{cases}, \tag{5b}$$

$$\Delta = \sqrt{(\lambda_a - \lambda_b)^2 + (\lambda_b - \lambda_c)^2 + (\lambda_a - \lambda_c)^2}, \tag{5c}$$

where the sector can be determined by three-phase power generation ratios [21].

2.2. Weighted Min-Max (WMM) Zero-Sequence Injection

The WMM zero-sequence injection [22, 23] was derived by modifying the conventional min-max zero-sequence injection for symmetrical three-phase converter output voltages:

$$v^0_{WMM} = -\frac{1}{2}\min\left\{\frac{\bar{\lambda}}{\lambda_a}v_a^+, \frac{\bar{\lambda}}{\lambda_b}v_b^+, \frac{\bar{\lambda}}{\lambda_c}v_c^+\right\} - \frac{1}{2}\max\left\{\frac{\bar{\lambda}}{\lambda_a}v_a^+, \frac{\bar{\lambda}}{\lambda_b}v_b^+, \frac{\bar{\lambda}}{\lambda_c}v_c^+\right\}. \tag{6}$$

Coefficients based on three-phase power generation ratios are included to account for the unequal power generation between the phases.

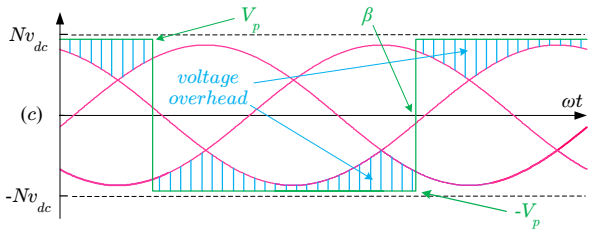

Fig. 3. *Optimal Zero-Sequence Injection (OZSI).*

2.3. Double 1/6 Third Harmonic Injection (DTHI)

DTHI [21] introduces a 1/6 third harmonic injection of both positive and fundamental frequency zero-sequence:

$$v^0_{DTHI} = \underbrace{v^0_{FF}}_{\text{Term 1}} - \underbrace{\frac{1}{6}\sqrt{2}V^+\cos\left(3\omega t + 3\alpha\right)}_{\text{Term 2}} - \underbrace{\frac{1}{6}\sqrt{2}V^0\cos\left(3\omega t + 3\theta\right)}_{\text{Term 3}}, \tag{7}$$

Term 1 stands for the fundamental frequency component of v^0_{DTHI}, which is identical to v^0_{FF}. Term 2 represents the 1/6 third harmonic injection of v^+_a, v^+_b, v^+_c, while Term 3 denotes the 1/6 third harmonic injection of v^0_{FF}.

2.4. Double Min-Max (DMM) Zero-Sequence Injection

Similar to the idea of DTHI, DMM zero-sequence injection [21] introduces the min-max sequence of the positive-sequence components, and the min-max sequence of v^0_{FF}:

$$v^0_{DMM} = \underbrace{v^0_{FF}}_{\text{Term 1}} + \left(\underbrace{\min\max\left\{v^+_a, v^+_b, v^+_c\right\}}_{\text{Term 2}}\right) + \left(\underbrace{\min\max\left\{v^0_{FF}, v^{0*}_{FF}, v^{0**}_{FF}\right\}}_{\text{Term 3}}\right). \tag{8}$$

Term 1 represents the fundamental frequency component of v^0_{DMM}, which is still identical to v^0_{FF}, while Terms 2 and 3 represent the min-max sequence ($\min\max = \frac{\max\left\{v^+_a, v^+_b, v^+_c\right\} + \min\left\{v^+_a, v^+_b, v^+_c\right\}}{2}$)) of the positive-sequence and v^0_{FF}, respectively. v^{0*}_{FF} and v^{0**}_{FF} are fictitious voltages created by displacing the fundamental frequency component v^0_{FF} by 120° and 240°, respectively.

2.5. Optimal Zero-Sequence Injection (OZSI)

An optimal method should satisfy two requirements [24]: (1) the fundamental frequency component of OZSI should be equal to v^0_{FF}, and (2) the peak value of the converter output voltages should be as low as possible to avoid saturation. The voltage overhead in Fig. 4 meets the two above mentioned requirements requirements.

The two required parameters to define the optimal sequence as shown in Fig. 4 are the positive-to-negative zero-crossing angle of the optimal zero sequence injection (β) and the magnitude of the square wave (V_p). These can be calculated by a fixed point iterative method and are calculated by (9) and (10) [24].

This article has been accepted for publication in a future issue of this journal, but has not been fully edited.
Content may change prior to final publication in an issue of the journal. To cite the paper please use the doi provided on the Digital Library page.

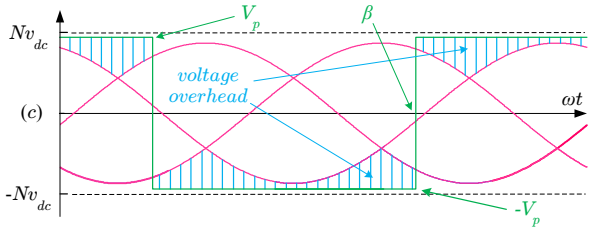

Fig. 4. *Optimal Zero-Sequence Injection (OZSI).*

$$\beta_{k+1} = \varphi(\beta_k) \qquad k = 0, 1, 2...$$

$$\begin{aligned}\varphi(\beta_k) = &-\frac{\sqrt{3}V^0}{3V^+}\cos(\beta_k+\alpha)\cot(\beta_k+\alpha) - \frac{\sqrt{3}\pi}{6}\cot(\beta_k+\alpha) + \frac{1}{2}\sin 2(\beta_k+\alpha) \\ &+\frac{1}{2}(\cos 2(\beta_k+\alpha)-1)\cot(\beta_k+\alpha) + \frac{\sqrt{3}V^0}{3V^+}\pi\sin(\theta+\alpha) + \frac{3\pi}{2} - \alpha\end{aligned} \quad , \tag{9}$$

$$V_p = \frac{\sqrt{6}V^+(\cos 2(\beta+\alpha)-1) - 2\sqrt{2}\pi V^0\cos(\theta-\alpha) - \sqrt{2}\pi V^+}{8\sin(\beta+\alpha)}. \tag{10}$$

.

3. Theoretical Comparison of Power Balance Capability

Power balance capability is defined as the ability of a zero-sequence injection method to deal with inter-phase power imbalance. Methods with superior power balance capability are able to generate three-phase balanced grid currents under severe power imbalances, whereas other methods fail.

The power generation of each phase fluctuates with changing solar irradiance and/or ambient temperature of the solar panels connected to that phase. Based on the definition of power generation ratios (1), the ratios can only vary between zero and one:

$$0 \le \lambda_a, \lambda_b, \lambda_c \le 1, \tag{11}$$

and hence all possible power imbalance cases fall within the unity cube $(1 \times 1 \times 1)$ of Fig. 5. Each power imbalance case can be represented by a unique operation point $(\lambda'_a, \lambda'_b, \lambda'_c)$ inside the cube.

If the maximum converter output voltage is lower than the total available dc-side voltage of one phase leg

$$\max\{v_a, v_b, v_c\}(\lambda'_a, \lambda'_b, \lambda'_c) \le Nv_{dc}, \tag{12}$$

then three-phase balanced grid currents can be generated without saturation, and this operation point can be rebalanced using a given method.

All operation points that can be rebalanced form a three-dimensional space, defined as the Power Balance Space (PBS). The volume of the PBS is defined as the Power Balance Factor (PBF)

$$PBF = \int_0^1\int_0^1\int_0^1 F(\lambda_a, \lambda_b, \lambda_c)\, d\lambda_a\, d\lambda_b\, d\lambda_c, \tag{13}$$

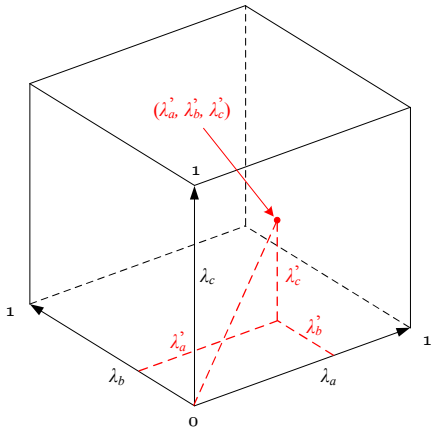

Fig. 5. *The unity cube.*

where

$$F(\lambda_a, \lambda_b, \lambda_c) = \begin{cases} 1, & \max\{v_a, v_b, v_c\}(\lambda_a, \lambda_b, \lambda_c) \leq N v_{dc} \\ 0, & \max\{v_a, v_b, v_c\}(\lambda_a, \lambda_b, \lambda_c) > N v_{dc} \end{cases}. \tag{14}$$

It is shown in the appendix that the presented PBS and PBF are only dependent on two normalized parameters, the per unit value of connection inductors $L_{f(p.u.)}$ and the voltage overrating ξ [1]. The per unit value of connection inductors $L_{f(p.u.)}$ is defined as

$$L_{f(p.u.)} = \frac{2\pi f L_f P_{nom}}{V_g^2}, \tag{15}$$

and the voltage overrating ξ is defined as the redundancy of the total available dc-side capacitor voltage to the maximum converter output voltage under nominal power operation

$$\xi = \frac{N v_{dc}}{\sqrt{2}\sqrt{1 + L_{f(p.u.)}^2}\frac{V_g}{\sqrt{3}}} - 1. \tag{16}$$

The previous concepts of the PBS and PBF in [26,27] require the absolute values of application-specific parameters, like the grid voltage V_g, three-phase nominal power P_{nom}, the dc-side capacitor voltage v_{dc} and the bridge number N for each iterative calculation. However, the revised definitions introduced in this paper are only dependent on two normalized parameters ($L_{f(p.u.)}$ and ξ), that only use the application-specific parameters in the definition of the overrating ξ. This new definition makes the results applicable to general cases without the need for continuous evaluation. Therefore, these metrics can provide the general assessment of the power balance capabilities of different zero-sequence injection methods, regardless of the application-specific characteristics.

The PBS of FFZSI is plotted in Fig. 6 for a CHB converter with $L_{f(p.u.)} = 0.05$ and 10% voltage overrating. All points lying within the PBS can be rebalanced by FFZSI, whereas all operation points outside the PBS are beyond the capability of FFZSI. The PBF of FFZSI is 4%, which means theoretically 4% of all possible power imbalance cases can be rebalanced by FFZSI.

[1]Note that in practical industrial applications, both voltage and current safety/tolerance margins are provided when designing the converter. However, in this paper, any voltage overrating refers only to voltage overrating needed to enhance the converter power balance capability.

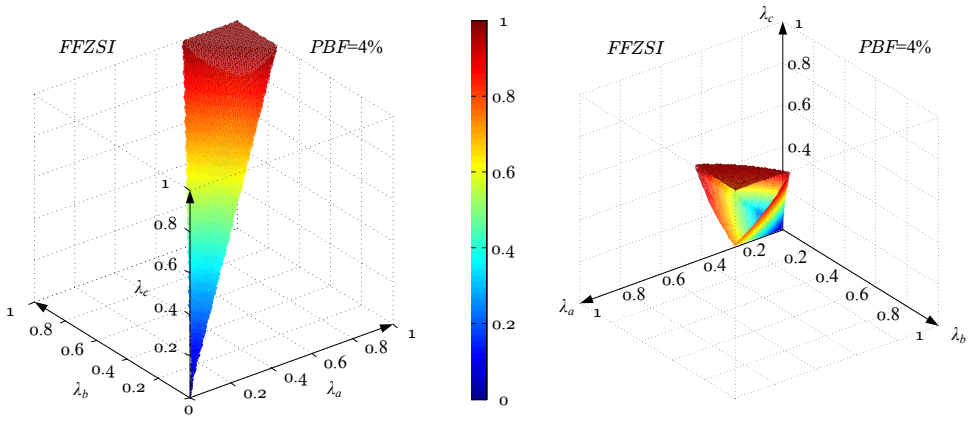

Fig. 6. *Power Balance Space of FFZSI for a CHB converter with* $L_{f(p.u.)} = 0.05$ *and 10% voltage overrating, viewed from different angles.*

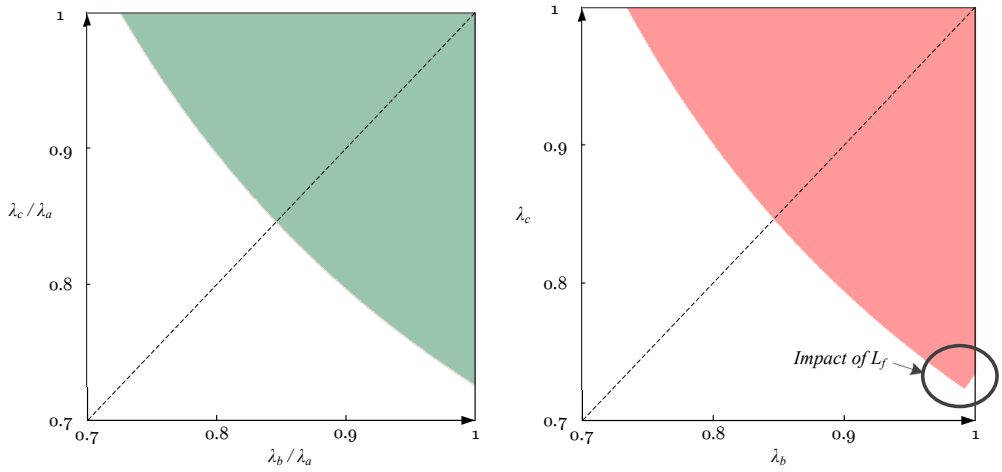

Fig. 7. *(a) Energy-Balancing Diagram (assuming* $(\lambda_a \geq \lambda_b \geq \lambda_c)$*) of [25]; (b) the cross section of the proposed PBS with the plane* $\lambda_a = 1$.

Fig. 7 shows that the two-dimensional Energy-Balancing Diagram (EBD) presented in [25] is the cross section of the proposed PBS with the plane $\lambda_a = 1$. The slight difference between Fig. 7(a) and (b) is due to the effect of connection inductors, which are neglected in the EBD of [25]. This difference increases as the size of the inductors also increases. The area of the diagram (Total Covered Area) [25] can be used to assess the power balance capabilities; however, it does not provide a clear idea of the percentage of viable cases which can be rebalanced among all possible power imbalance cases. The concept of PBF presented in this paper quantifies this percentage. Additionally, the EBD in Fig. 7(a) is based on relative power generation ratios of two phases (phases b and c in this case) with respect to the most productive phase (phase a in this case). This means that the generalized case $(\lambda'_a, \lambda'_b, \lambda'_c)$ is assumed to be equivalent to the chosen example of $(0.5\lambda'_a, 0.5\lambda'_b, 0.5\lambda'_c)$, which is not true when the effect of connection inductors, albeit typically small, is considered.

The PBSs of WMM, DTHI, DMM, and OZSI for a CHB converter with $L_{f(p.u.)} = 0.05$ and

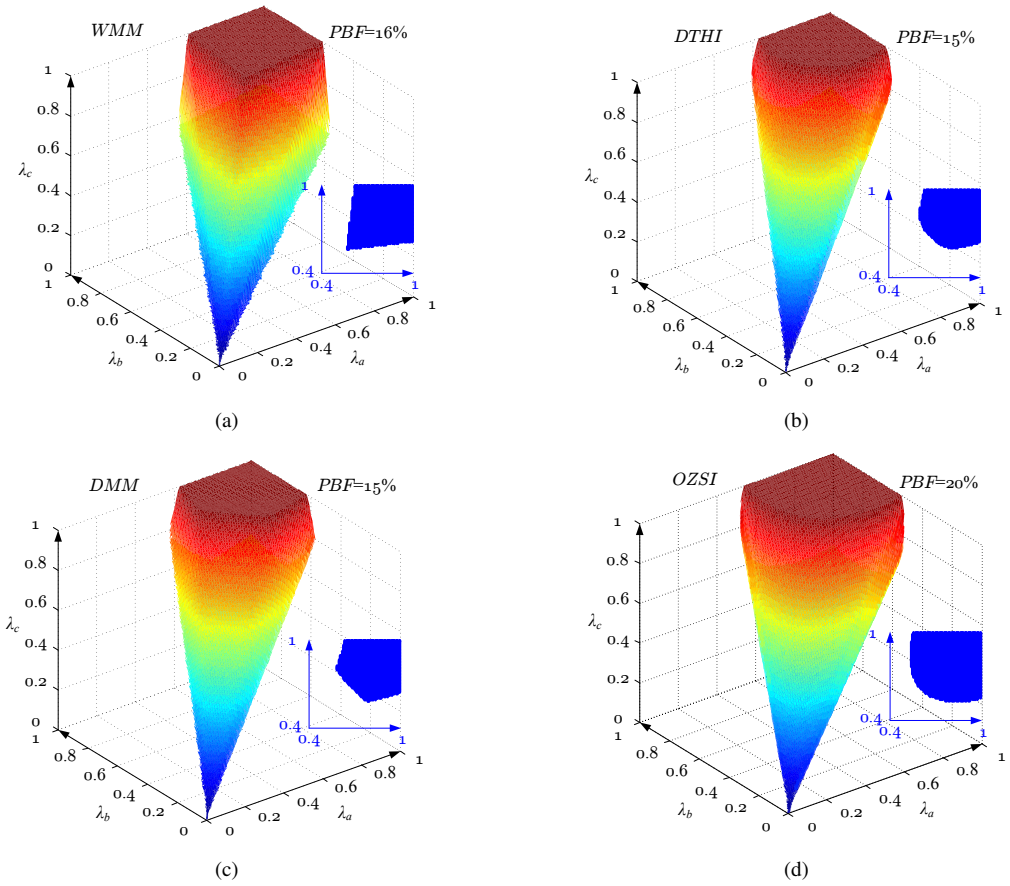

Fig. 8. *Power Balance Spaces and Energy-Balancing Diagrams of: (a) WMM, (b) DTHI, (c) DMM, and (d) OZSI for a CHB converter with* $L_{f(p.u.)} = 0.05$ *and 10% voltage overrating.*

10% voltage overrating are plotted in Fig. 8, as well as their Energy-Balancing Diagrams. Results show that WMM, DTHI, and DMM can generate balanced three-phase grid currents under approximately 15% of all possible power imbalance cases, whereas FFZSI can only rebalance 4%. OZSI can cope with up to 20% of cases. Therefore, with the same $L_{f(p.u.)}$ and voltage overrating ξ, WMM, DTHI, and DMM feature superior power balance capabilities compared to FFZSI, while OZSI has the best performance.

Fig. 9 shows the effects of $L_{f(p.u.)}$ and ξ on the PBF. It can be seen that higher voltage overrating significantly improves the PBF, which is expected because a higher total available dc-side capacitor voltage results in a converter less likely to saturate. Inductors have a limited yet practical impact on the PBF especially in the typical range $\left(L_{f(p.u.)} < 0.1\right)$ used in multilevel converters. Based on this result, we can conclude that the impact of inductors can be omitted in an initial calculation (e.g. during the initial design process) and accounted for in later detailed iterations. The voltage waveforms of FFZSI, WMM, DTHI, DMM and OZSI for a CHB converter designed with $L_{f(p.u.)} = 0.05$ are illustrated in Fig. 10, under one power imbalance case $(\lambda_a = 0.8, \lambda_b = 1, \lambda_c = 1)$.

3.1. Inaccuracy of Weighted Min-Max

It can be observed from Fig. 10(b) that the fundamental frequency component of WMM is different to that of other methods. As shown in the phasor diagram of Fig. 2, the fundamental frequency

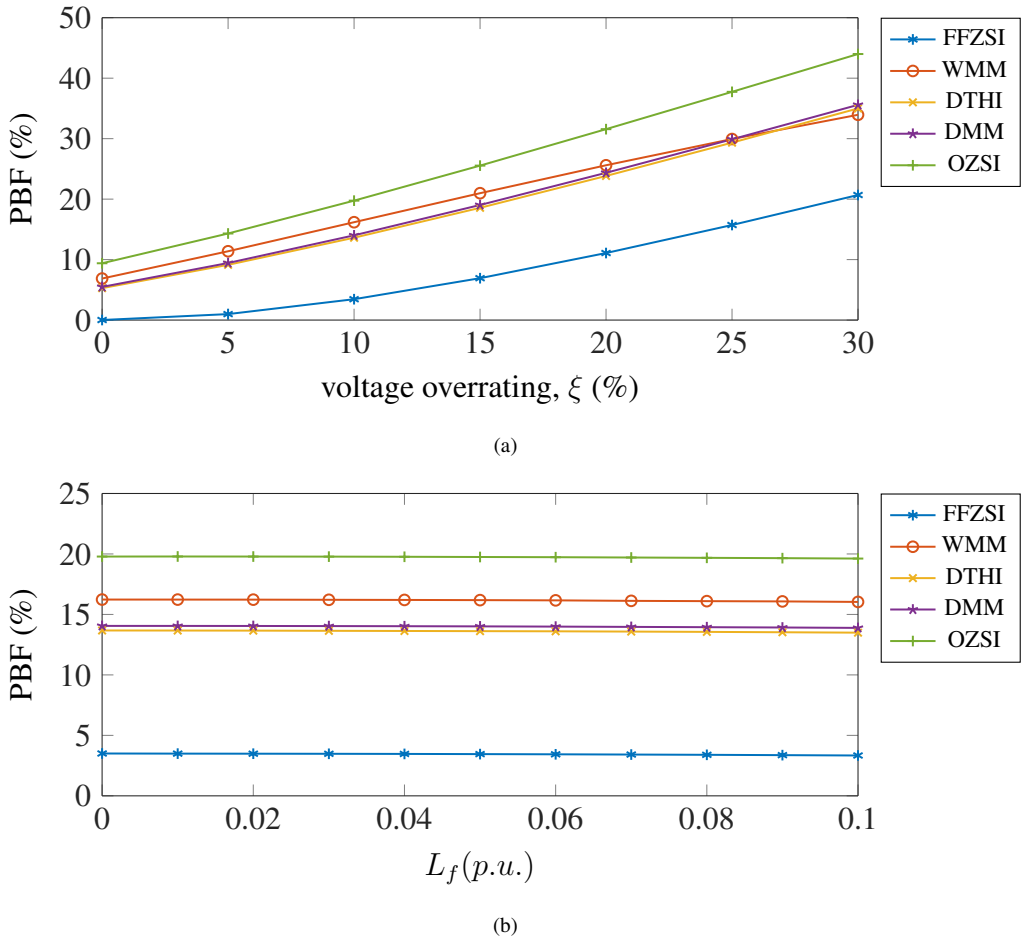

Fig. 9. *Power Balance Factors of FFZSI, WMM, DTHI, DMM, and OZSI of a CHB converter with (a)* $L_{f(p.u.)} = 0.05$ *and different voltage overratings and (b) 10% voltage overrating and different inductance values* $L_{f(p.u.)}$.

component of the zero-sequence voltage generates different amounts of power with the three-phase grid currents $\mathbf{I_{ga}}$ $\mathbf{I_{gb}}$ $\mathbf{I_{gc}}$, in accordance to $\lambda_a, \lambda_b, \lambda_c$ [21]. If the harmonic components of the grid currents are negligible, the harmonic components generated by the zero-sequence injection do not contribute to power rebalance. This is why DTHI, DMM and OZSI are derived by ensuring the same fundamental frequency component and modifying the harmonic components only [21, 24]. However, WMM was derived by modifying the conventional min-max zero-sequence injection with coefficients based on three-phase power generation ratios (6), which may not have the same fundamental frequency component.

This section calculates the fundamental frequency component of WMM, and explains how the control implementation in [23, 24] compensates any resulting inaccuracy. The voltage waveform of WMM over one fundamental period, as depicted in Fig. 11, can be expressed in a piecewise

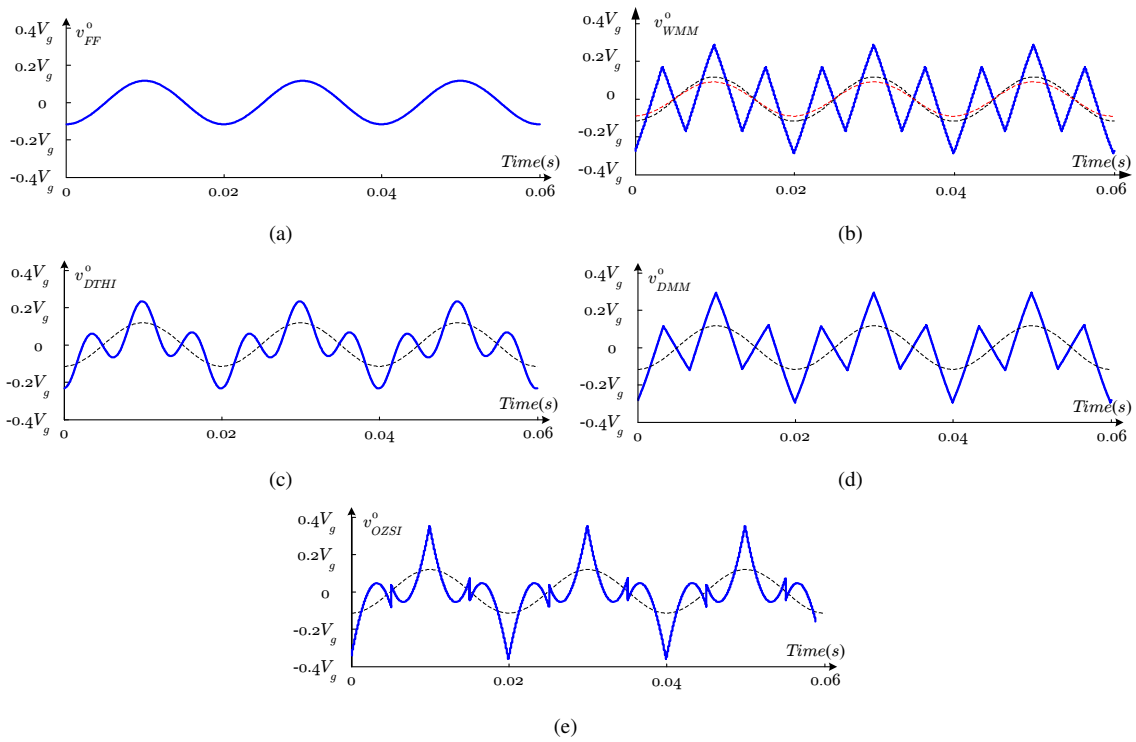

Fig. 10. *The waveforms of different zero-sequence injection methods and the corresponding fundamental frequency component under the power imbalance case* $(\lambda_a = 0.8, \lambda_b = 1, \lambda_c = 1)$*: (a) FFZSI, (b) WMM, (c) DTHI, (d) DMM, (e) OZSI.*

manner:

$$v^0_{WMM}(\omega t) = \begin{cases} -\dfrac{\bar{\lambda}}{2\lambda_a}V^+\cos(\omega t+\alpha) - \dfrac{\bar{\lambda}}{2\lambda_c}V^+\cos(\omega t+\alpha+2\pi/3) & 0 \le \omega t < \sigma_1-\alpha \\ -\dfrac{\bar{\lambda}}{2\lambda_b}V^+\cos(\omega t+\alpha-2\pi/3) - \dfrac{\bar{\lambda}}{2\lambda_c}V^+\cos(\omega t+\alpha+2\pi/3) & \sigma_1-\alpha \le \omega t < \sigma_2-\alpha \\ -\dfrac{\bar{\lambda}}{2\lambda_b}V^+\cos(\omega t+\alpha-2\pi/3) - \dfrac{\bar{\lambda}}{2\lambda_a}V^+\cos(\omega t+\alpha) & \sigma_2-\alpha \le \omega t < \sigma_3-\alpha \\ -\dfrac{\bar{\lambda}}{2\lambda_c}V^+\cos(\omega t+\alpha+2\pi/3) - \dfrac{\bar{\lambda}}{2\lambda_a}V^+\cos(\omega t+\alpha) & \sigma_3-\alpha \le \omega t < \sigma_4-\alpha \\ -\dfrac{\bar{\lambda}}{2\lambda_c}V^+\cos(\omega t+\alpha+2\pi/3) - \dfrac{\bar{\lambda}}{2\lambda_b}V^+\cos(\omega t+\alpha-2\pi/3) & \sigma_4-\alpha \le \omega t < \sigma_5-\alpha \\ -\dfrac{\bar{\lambda}}{2\lambda_a}V^+\cos(\omega t+\alpha) - \dfrac{\bar{\lambda}}{2\lambda_b}V^+\cos(\omega t+\alpha-2\pi/3) & \sigma_5-\alpha \le \omega t < \sigma_6-\alpha \\ -\dfrac{\bar{\lambda}}{2\lambda_a}V^+\cos(\omega t+\alpha) - \dfrac{\bar{\lambda}}{2\lambda_c}V^+\cos(\omega t+\alpha+2\pi/3) & \sigma_6-\alpha \le \omega t < 2\pi \end{cases}, \tag{17}$$

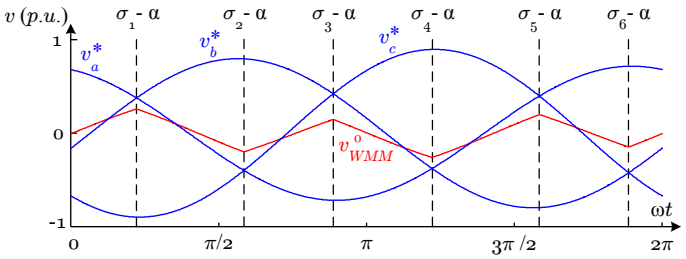

Fig. 11. *WMM waveform over one fundamental period* $(\lambda_a > \lambda_b > \lambda_c)$ $\left(v_a^* = \bar{\lambda} v_a^+/\lambda_a, v_b^* = \bar{\lambda} v_b^+/\lambda_b, v_c^* = \bar{\lambda} v_c^+/\lambda_c\right)$.

where:

$$\sigma_1 = \arctan\frac{\lambda_a + 2\lambda_b}{\sqrt{3}\lambda_a}, \quad \sigma_4 = \sigma_1 + \pi, \tag{18a}$$

$$\sigma_2 = \pi - \arctan\frac{\lambda_a + 2\lambda_c}{\sqrt{3}\lambda_a}, \quad \sigma_5 = \sigma_2 + \pi, \tag{18b}$$

$$\sigma_3 = \pi - \arctan\frac{\lambda_b - \lambda_c}{\sqrt{3}\left(\lambda_b + \lambda_c\right)}, \quad \sigma_6 = \sigma_3 + \pi. \tag{18c}$$

The fundamental frequency component of v_{WMM}^0 can be calculated as:

$$v_{WMM(f)}^0 = \sqrt{2} V_{WMM(f)}^0 \cos\left(\omega t + \theta'\right), \tag{19}$$

where:

$$V_{WMM(f)}^0 = \sqrt{a_1^2 + b_1^2}/\sqrt{2}, \quad \tan\theta' = -\frac{b_1}{a_1}. \tag{20}$$

The coefficients a_1 and b_1 can be written as:

$$a_1 = \frac{1}{\pi}\int_{-\pi}^{\pi} v_{WMM}^0 \cos\omega t \,\mathrm{d}\omega t = \frac{1}{\pi}\int_{0}^{2\pi} v_{WMM}^0 \cos\omega t \,\mathrm{d}\omega t = m\cos\alpha + n\sin\alpha, \tag{21}$$

$$b_1 = \frac{1}{\pi}\int_{-\pi}^{\pi} v_{WMM}^0 \sin\omega t \,\mathrm{d}\omega t = \frac{1}{\pi}\int_{0}^{2\pi} v_{WMM}^0 \sin\omega t \,\mathrm{d}\omega t = n\cos\alpha - m\sin\alpha, \tag{22}$$

where:

$$m = -\frac{\sqrt{2}\bar{\lambda}V^+}{2\pi}\left\{\frac{1}{\lambda_a}(\sigma_1 - \sigma_2 + \pi) - \frac{1}{2\lambda_b}(\sigma_3 - \sigma_1) - \frac{1}{2\lambda_c}(\sigma_2 - \sigma_3 + \pi) + \frac{1}{2\lambda_a}(\sin 2\sigma_1 - \sin 2\sigma_2)\right.$$
$$\left. + \frac{1}{2\lambda_b}\left[\sin\left(2\sigma_3 - 2\pi/3\right) - \sin\left(2\sigma_1 - 2\pi/3\right)\right] + \frac{1}{2\lambda_c}\left[\sin\left(2\sigma_2 + 2\pi/3\right) - \sin\left(2\sigma_3 + 2\pi/3\right)\right]\right\}, \tag{23}$$

$$n = \frac{\sqrt{2}\bar{\lambda}V^+}{2\pi}\left\{-\frac{\sqrt{3}}{2\lambda_b}(\sigma_3 - \sigma_1) + \frac{\sqrt{3}}{2\lambda_c}(\sigma_2 - \sigma_3 + \pi) + \frac{1}{2\lambda_a}(\cos 2\sigma_1 - \cos 2\sigma_2)\right.$$
$$\left. + \frac{1}{2\lambda_b}\left[\cos\left(2\sigma_3 - 2\pi/3\right) - \cos\left(2\sigma_1 - 2\pi/3\right)\right] + \frac{1}{2\lambda_c}\left[\cos\left(2\sigma_2 + 2\pi/3\right) - \cos\left(2\sigma_3 + 2\pi/3\right)\right]\right\}. \tag{24}$$

This article has been accepted for publication in a future issue of this journal, but has not been fully edited.
Content may change prior to final publication in an issue of the journal. To cite the paper please use the doi provided on the Digital Library page.

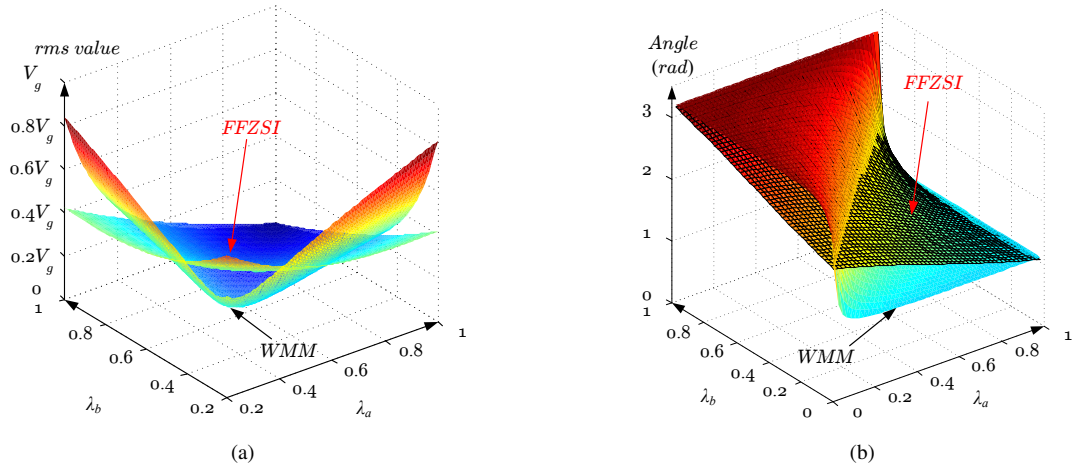

Fig. 12. *Difference between the fundamental frequency component of WMM and FFZSI for a CHB converter with $L_{f(p.u.)} = 0.05$ (a) rms value (b) phase angle.*

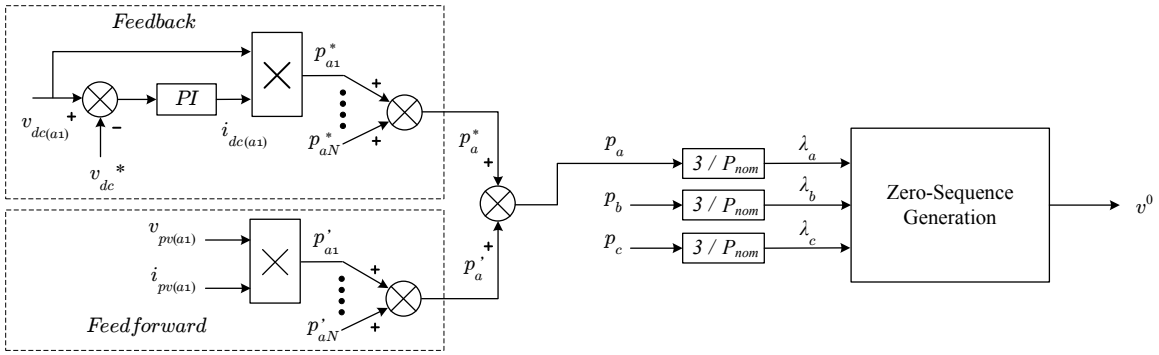

Fig. 13. *Control implementation of the zero-sequence generation.*

Equations (26)-(33) show that the *rms* value and phase angle of $v^0_{WWM(f)}$ are only dependent on V_g and $L_{f(p.u.)}$, under a specific power imbalance case. The *rms* value and phase angle of $v^0_{WWM(f)}$ are plotted in Fig. 12 as well as those of v^0_{FF}, for a CHB converter with $L_{f(p.u.)} = 0.05$. In the figure, λ_c is always equal to 1 to allow three-dimensional illustration. It can be seen that the *rms* values of $v^0_{WWM(f)}$ and v^0_{FF} are generally unequal, and the difference increases dramatically as the power imbalance becomes severe. When the power generation level of one phase approaches zero, the *rms* value of WMM tends to infinity according to (6), and the error thus becomes very significant. The phase angles are also generally unequal.

The *rms* value and phase angle errors show that the fundamental frequency component of WMM deviates from the required component of (4) and (5). However, the control implementation proposed in [23,24], and shown in Fig. 13, can help eliminate the effect caused by any error. In Fig. 13, the three-phase power generation ratios λ_a, λ_b, λ_c, used to calculate the zero-sequence component, are obtained via a combination of feedforward and feedback control loops. The feedforward loop measures the output voltages and currents of PV arrays, and estimates the amount of power generated in each phase. The feedback loop, which compares the measured dc-side capacitor voltages to the reference, provides compensation for disparity in losses and other non-ideal factors.

When the injected zero-sequence has the correct fundamental frequency component (as with

FFZSI, DTHI, DMM and OZSI), the compensation generated by the feedback loop is quite small. When the fundamental frequency component of the injected zero-sequence deviates from the required value (as with WMM), the feedback loop drives the fundamental frequency component of the injected zero-sequence towards the required value. For example, if less power is extracted from phase a than is required, as a result of inaccurate fundamental frequency component of the zero-sequence injection technique, the capacitor voltages in phase a tend to increase. Therefore, λ_a seen from the zero-sequence generation block in Fig. 13 increases and the fundamental frequency component of the injected zero-sequence changes, until it extracts the correct amount of power from phase a.

Although the feedback loop can successfully drive the fundamental frequency component of the zero-sequence towards the correct value, the dynamic performance of the system deteriorates. This is because, when the amplitude and phase angle errors in Fig. 12 are significant, the information provided by the feedforward loop has a large error, meaning the dynamic behaviour almost entirely relies on the bandwidth of the feedback loop. However, the bandwidth of the feedback loop is limited, due to the need to minimize control interactions between cascaded control loops in a multilevel converter. Therefore, WMM may not be a suitable choice in applications where severe power imbalance cases must be compensated for, owing to its inaccurate fundamental frequency component.

4. Experimental Results

Experimental results validating the superiority of WMM, DTHI, DMM and OZSI over FFZSI have been provided in [21, 24]. In this paper, the results obtained from a 430 V, 10 kW, three-phase, seven-level CHB prototype verify that OZSI has superior power balance performance compared to WMM, DTHI and DMM, in accordance to the theoretical comparison.

The prototype in Fig. 14 consists of nine APS Powerex IGBT H-bridge modules (PP75B060) rated at 600 V and 75 A (three per phase), each of which is fed by a programmable PV simulator. The converter parameters are summarized in Table 1. The filtering inductors are quite large in the experiment $\left(L_{f(p.u.)} = 0.14\right)$, because there are only three bridges in the phase leg. In industrial CHB converters, inductors can be significantly reduced, while still achieving excellent harmonic performance, by cascading more bridges.

Table 1 Experimental Prototype Parameters

Parameters	Values
Grid Voltage, V_g	430 V
Three-phase Nominal Power, P_{nom}	10 kW
Three-phase Filtering Inductors (per phase), L_f	8 mH (0.14 p.u.)
MPP of PV Simulators	141.5 V, 7.88 A
dc-side Capacitor Voltage, v_{dc}	141.5 V
Carrier Frequency (PSPWM), f_s	600 Hz

The dc-dc conversion stage is not included. The converter thus only tracks the Maximum Power Point (MPP) under a solar irradiance of 1000 W/m^2 and an ambient temperature of 25°C. Although the converter lacks the ability to track the MPP when either the solar irradiance or the ambient temperature changes, it does not affect the purpose of the experiment, which is to compare different

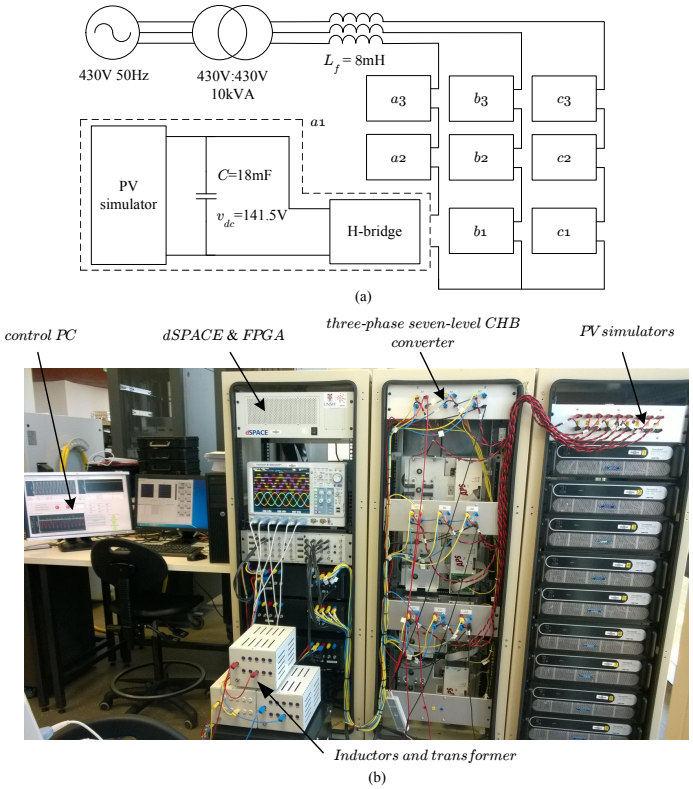

Fig. 14. *The experimental setup: (a) schematic diagram and (b) hardware setup.*

zero-sequence injection methods, as long as the created power imbalance cases are identical.

The solar irradiance associated with the PV simulators of phase a was programmed to decrease from 1000 W/m^2 to 500 W/m^2, while the irradiance in the other two phases remained unchanged at 1000 W/m^2. As a result, the power generation of phase a fell to approximately 50% of its nominal value $(\lambda_a \approx 0.5)$. The converter output voltages and grid currents for WMM, DTHI, and DMM are shown in Fig. 15(a)-(c), respectively. All three methods are unable to provide satisfactory three-phase grid currents, because the power imbalance case $(\lambda_a \approx 0.5, \lambda_b = 1, \lambda_c = 1)$ lies outside of their PBSs. OZSI, on the other hand, is still able to generate three-phase balanced grid currents (Fig. 15(d)). Therefore, the superiority of OZSI over the other three methods (WMM, DTHI, and DMM) in the case of severe power imbalance is validated.

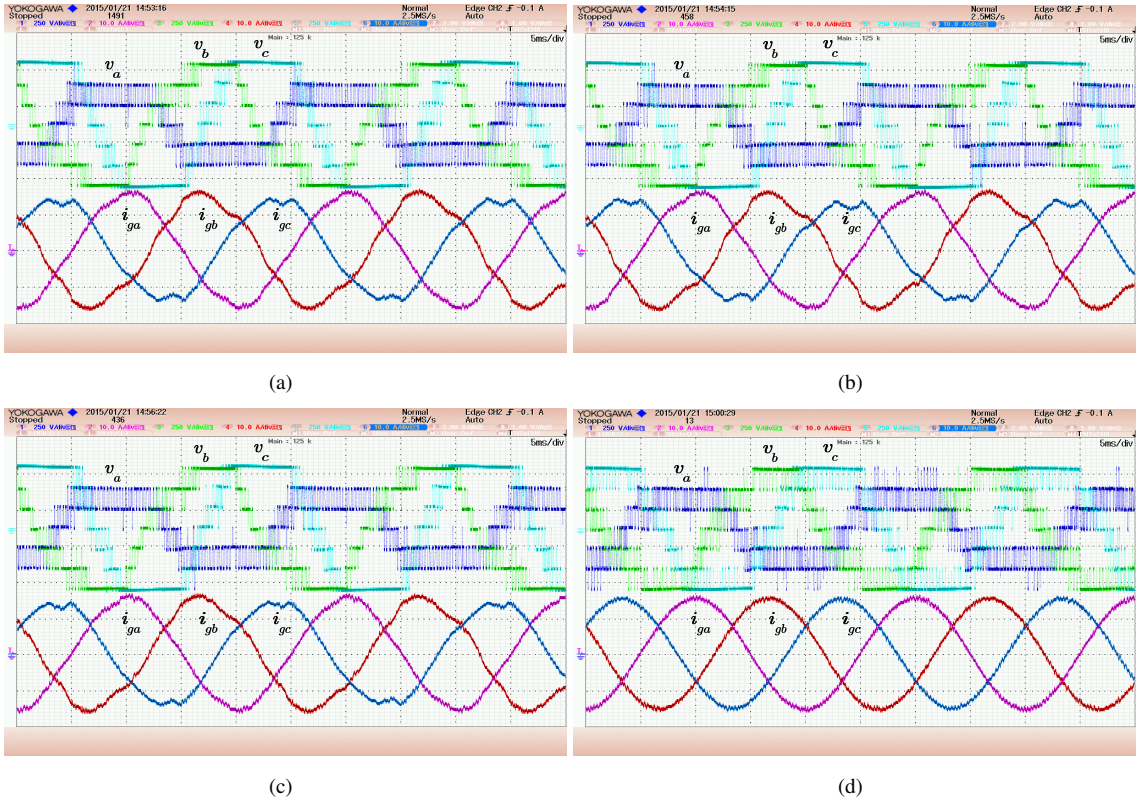

Fig. 15. *Experimental converter output voltages and grid currents with (a) WMM, (b) DTHI, (c) DMM, (d) OZSI. CH1: converter output voltage of phase a, v_a; CH2: grid current of phase a, i_{ga}; CH3: converter output voltage of phase b, v_b; CH4: grid current of phase b, i_{gb}; CH5: converter output voltage of phase c, v_c; CH6: grid current of phase c, i_{gc}. CH1, CH3, CH5: 250 V/div; CH2, CH4, CH6: 10 A/div.*

5. Conclusion & Discussion

This paper provides theoretical comparison of power balance capabilities of various zero-sequence injection methods based on two metrics which can be easily generalized for all applications.

Table 2 Zero Sequence Injection Methods Relative Performance Summary [2]

Methods	Accuracy	Complexity	Power Balance Capability	Imbalance Energy Loss
FFZSI	✓✓	✓✓	✗	✗
WMM	✗	✓✓	✓	✓
DTHI	✓✓	✓	✓	✓
DMM	✓✓	✓	✓	✓
OZSI	✓✓	✓	✓✓	✓✓

[2] ✓✓: Optimal, ✓: Satisfactory, ✗: Unsatisfactory

The comparative performance of the methods is summarized in Table 2 and the following conclusions can be derived:

- FFZSI, DTHI, RTHI, DMM and OZSI are accurate, whereas WMM and SOZSI may introduce some errors.
- FFZSI, WMM, DTHI and DMM feature simple implementation, whereas OZSI and SOZSI are complex, yet still acceptable for the real time implementation. RTHI, on the other hand, is too complex to implement in most cases.
- FFZSI has the basic power balance capability, whereas WMM, DTHI, RTHI and DMM feature advanced performance. The power balance capability of OZSI and SOZSI is superior.
- The comparison of imbalance energy losses confirms that OZSI and SOZSI are superior to other methods, followed by WMM, DTHI, RTHI and DMM. FFZSI, once more, exhibits the worst performance.

Overall, OZSI is favored in applications where severe power imbalance occurs frequently, because of its superior power balance capability. For less demanding applications, either DTHI or DMM should be the best choice, owing to their simplicity. Finally, experimental results based on a 430 V, 10 kW, three-phase, seven-level cascaded H-bridge converter prototype are provided to confirm the superior performance of the optimal zero-sequence injection.

6. Appendices

In the Appendix, we prove that the presented PBS and PBF are only dependent on two normalized parameters, the per unit value of connection inductors $L_{f(p.u.)}$ and the voltage overrating ξ, defined in (15) and (16).

Based on the definitions of PBS and PBF, we first need to prove that the relationship in (14) between *(a)* the maximum converter output voltage of any operation point

$$(\max\{v_a, v_b, v_c\}(\lambda_a, \lambda_b, \lambda_c))$$

and *(b)* the total available dc-side capacitor voltage Nv_{dc}, is only dependent on $L_{f(p.u.)}$ and ξ.

6.1. Maximum Converter Output Voltage

Using FFZSI as an example, the converter output voltages v_a, v_b, v_c of a generalized operation point consist of *(a)* positive-sequence component v_a^+, v_b^+, v_c^+ and *(b)* zero-sequence component v_{FF}^0

$$v_a = v_a^+ + v_{FF}^0, \tag{25a}$$
$$v_b = v_b^+ + v_{FF}^0, \tag{25b}$$
$$v_b = v_c^+ + v_{FF}^0. \tag{25c}$$

6.1.1. Positive-Sequence: The positive-sequence can be determined as if the three-phase power generation levels were equal

$$v_a^+ = \sqrt{2}V^+\cos(\omega t + \alpha), \tag{26a}$$
$$v_b^+ = \sqrt{2}V^+\cos(\omega t + \alpha - 2\pi/3), \tag{26b}$$
$$v_c^+ = \sqrt{2}V^+\cos(\omega t + \alpha + 2\pi/3). \tag{26c}$$

where

$$V^+ = \sqrt{\left(\frac{V_g}{\sqrt{3}}\right)^2 + \left(2\pi f L_f \frac{\lambda'_a + \lambda'_b + \lambda'_b}{3} \frac{P_{nom}}{\sqrt{3}V_g}\right)^2}, \tag{27}$$

$$\alpha = \tan^{-1}\left(\frac{2\pi f L_f \frac{\lambda'_a + \lambda'_b + \lambda'_c}{3} \frac{P_{nom}}{\sqrt{3}V_g}}{\frac{V_g}{\sqrt{3}}}\right). \tag{28}$$

Based on the definition of $L_{f(p.u.)}$ in (15), both V^+ and α can be rearranged as

$$V^+ = \sqrt{1 + \left(\frac{\lambda'_a + \lambda'_b + \lambda'_c}{3} L_{f(p.u.)}\right)^2} \frac{V_g}{\sqrt{3}}, \tag{29}$$

$$\alpha = \tan^{-1}\left(\frac{\lambda'_a + \lambda'_b + \lambda'_c}{3} L_{f(p.u.)}\right), \tag{30}$$

and the positive-sequence of a generalized operation point becomes functions of $L_{f(p.u.)}$ and the grid voltage V_g

$$\begin{aligned} v_a^+ &= \sqrt{2}\sqrt{1 + \left(\frac{\lambda'_a + \lambda'_b + \lambda'_c}{3} L_{f(p.u.)}\right)^2} \frac{V_g}{\sqrt{3}} \cos\left(\omega t + \tan^{-1}\left(\frac{\lambda'_a + \lambda'_b + \lambda'_c}{3} L_{f(p.u.)}\right)\right), \\ &= V_g F_1\left(L_{f(p.u.)}\right) \cos\left(\omega t + F_2\left(L_{f(p.u.)}\right)\right) \end{aligned} \tag{31a}$$

$$\begin{aligned} v_b^+ &= \sqrt{2}\sqrt{1 + \left(\frac{\lambda'_a + \lambda'_b + \lambda'_c}{3} L_{f(p.u.)}\right)^2} \frac{V_g}{\sqrt{3}} \cos\left(\omega t + \tan^{-1}\left(\frac{\lambda'_a + \lambda'_b + \lambda'_c}{3} L_{f(p.u.)}\right) - 2\pi/3\right), \\ &= V_g F_3\left(L_{f(p.u.)}\right) \cos\left(\omega t + F_4\left(L_{f(p.u.)}\right)\right) \end{aligned} \tag{31b}$$

$$\begin{aligned} v_b^+ &= \sqrt{2}\sqrt{1 + \left(\frac{\lambda'_a + \lambda'_b + \lambda'_c}{3} L_{f(p.u.)}\right)^2} \frac{V_g}{\sqrt{3}} \cos\left(\omega t + \tan^{-1}\left(\frac{\lambda'_a + \lambda'_b + \lambda'_c}{3} L_{f(p.u.)}\right) + 2\pi/3\right). \\ &= V_g F_5\left(L_{f(p.u.)}\right) \cos\left(\omega t + F_6\left(L_{f(p.u.)}\right)\right) \end{aligned} \tag{31c}$$

6.1.2. Zero-Sequence: The zero-sequence v_{FF}^0 of the same operating point can be determined based on the power generation ratios as (4):

$$v_{FF}^0 = \sqrt{2}\frac{\sqrt{6}\Delta}{3(\lambda'_a + \lambda'_b + \lambda'_c)} V_g \cos(\omega t + \theta), \tag{32}$$

where

$$\theta = \begin{cases} \sin^{-1}\left(\dfrac{\sqrt{6}\left(\lambda'_c - \lambda'_b\right)}{2\Delta}\right) & \text{Sectors (I), (VI)} \\ \dfrac{2\pi}{3} + \sin^{-1}\left(\dfrac{\sqrt{6}\left(\lambda'_b - \lambda'_a\right)}{2\Delta}\right) & \text{Sectors (II), (III)} \\ \dfrac{4\pi}{3} + \sin^{-1}\left(\dfrac{\sqrt{6}\left(\lambda'_a - \lambda'_c\right)}{2\Delta}\right) & \text{Sectors (IV), (V)} \end{cases}, \tag{33a}$$

$$\Delta = \sqrt{\left(\lambda'_a - \lambda'_b\right)^2 + \left(\lambda'_b - \lambda'_c\right)^2 + \left(\lambda'_a - \lambda'_c\right)^2}, \tag{33b}$$

As a result, the zero-sequence of a generalized operation point also becomes a function of the grid voltage V_g

$$v^0_{FF} = V_g K_1\left(\lambda'_a, \lambda'_b, \lambda'_c\right)\cos\left(\omega t + K_2\left(\lambda'_a, \lambda'_b, \lambda'_c\right)\right), \tag{34}$$

where K_1 and K_2 are constants for a specific operation point.

Therefore, the converter output voltages v_a, v_b, v_c of a generalized operation point can be rewritten as

$$v_a = v^+_a + v^0_{FF} = V_g\left[F_1\left(L_{f(p.u.)}\right)\cos\left(\omega t + F_2\left(L_{f(p.u.)}\right)\right) + K_1\cos\left(\omega t + K_2\right)\right], \tag{35a}$$

$$v_b = v^+_b + v^0_{FF} = V_g\left[F_3\left(L_{f(p.u.)}\right)\cos\left(\omega t + F_4\left(L_{f(p.u.)}\right)\right) + K_1\cos\left(\omega t + K_2\right)\right], \tag{35b}$$

$$v_b = v^+_c + v^0_{FF} = V_g\left[F_5\left(L_{f(p.u.)}\right)\cos\left(\omega t + F_6\left(L_{f(p.u.)}\right)\right) + K_1\cos\left(\omega t + K_2\right)\right], \tag{35c}$$

and the maximum converter output voltage of a generalized operation point becomes a function of $L_{f(p.u.)}$ and V_g

$$\max\left\{v_a, v_b, v_c\right\}\left(\lambda'_a, \lambda'_b, \lambda'_c\right) = V_g F_7\left(L_{f(p.u.)}\right). \tag{36}$$

6.2. *Total Available dc-side Capacitor Voltage*

Based on the definition of the voltage overrating ξ in (16), the total available dc-side capacitor voltage can be represented as

$$Nv_{dc} = \sqrt{2}\sqrt{1 + L^2_{f(p.u.)}}\frac{V_g}{\sqrt{3}}\left(\xi + 1\right). \tag{37}$$

Therefore, the relationship in (14) between (a) the maximum converter output voltage of a generalized operation point $\left(\max\left\{v_a, v_b, v_c\right\}\left(\lambda_a, \lambda_b, \lambda_c\right)\right)$ and (b) the total available dc-side capacitor voltage Nv_{dc}, is only dependent on $L_{f(p.u.)}$ and ξ

$$\max\left\{v_a, v_b, v_c\right\}\left(\lambda'_a, \lambda'_b, \lambda'_c\right) \le Nv_{dc} \iff F_7\left(L_{f(p.u.)}\right) \le \frac{\sqrt{2}}{\sqrt{3}}\sqrt{1 + L^2_{f(p.u.)}}\left(\xi + 1\right), \tag{38}$$

regardless of the absolute values of the grid voltage V_g, three-phase nominal power P_{nom}, the dc-side capacitor voltage v_{dc} and the bridge number N.

7. References

[1] J. M. Carrasco, L. G. Franquelo, J. T. Bialasiewicz, E. Galvan, R. C. P. Guisado, M. A. M. Prats, J. I. Leon, and N. Moreno-Alfonso, "Power-electronic systems for the grid integration of renewable energy sources: a survey," *IEEE Trans. Ind. Electron.*, vol. 53, no. 4, pp. 1002–1016, Jun. 2006.

[2] J. Mei, B. Xiao, K. Shen, L. M. Tolbert, and J. Zheng, "Modular multilevel inverter with new modulation method and its application to photovoltaic grid-connected generator," *IEEE Trans. Power Electron.*, vol. 28, no. 11, pp. 5063–5073, Nov. 2013.

[3] G. Grandi, C. Rossi, D. Ostojic, and D. Casadei, "A new multilevel conversion structure for grid-connected PV applications," *IEEE Trans. Ind. Electron.*, vol. 56, no. 11, pp. 4416–4426, Nov. 2009.

[4] Y. Zhou, and H. Li, "Analysis and suppression of leakage current in cascaded-multilevel-inverter-based PV systems," *IEEE Trans. Power Electron.*, vol. 29, no. 10, pp. 5265–5277, Oct. 2014.

[5] D. Sun, B. Ge, X. Yan, D. Bi, H. Zhang, Y. Liu, H. Abu-Rub, L. Ben-Brahim, and F. Z. Peng, "Modeling, impedance design, and efficiency analysis of quasi-Z-Source module in cascaded multilevel photovoltaic power system," *IEEE Trans. Ind. Electron.*, vol. 61, no. 11, pp. 6108–6117, Nov. 2014.

[6] Y. Liu, B. Ge and H. Abu-Rub, "Modelling and controller design of quasi-Z-source cascaded multilevel inverter-based three-phase grid-tie photovoltaic power system," *IET Renewable Power Generation*, vol. 8, no. 8, 2014, pp. 925–936.

[7] A. Alexander, M. Thathan, "Modelling and analysis of modular multilevel converter for solar photovoltaic applications to improve power quality", *IET Renewable Power Generation*, vol. 9, no. 1, 2015, pp. 77-88.

[8] S. Essakiappan, H. S. Krishnamoorthy, P. Enjeti, R. S. Balog, and S. Ahmed, "Multilevel medium frequency link inverter for utility scale photovoltaic integration," *IEEE Trans. Power Electron.*, vol. 30, no. 7, pp. 3674–3684, Jul. 2015.

[9] Y. Liu, B. Ge, H. Abu-Rub, and F. Z. Peng, "An effective control method for three-phase quasi-Z-source cascaded multilevel inverter based grid-tie photovoltaic power system," *IEEE Trans. Ind. Electron.*, vol. 61, no. 12, pp. 6794–6802, Dec. 2014.

[10] O. Alonso, P. Sanchis, E. Gubia, and L. Marroyo, "Cascaded H-bridge multilevel converter for grid connected photovoltaic generators with independent maximum power point tracking of each solar array," in *Proc. IEEE PESC 2003*, pp. 731–735.

[11] J. Sastry, P. Bakas, H. Kim, L. Wang, and A. Marinopoulos, "Evaluation of cascaded H-bridge inverter for utility-scale photovoltaic systems," *Renewable Energy*, vol. 69, pp. 208–218, Sep. 2014.

[12] E. Villanueva, P. Correa, J. Rodriguez, and M. Pacas, "Control of a single-phase cascaded H-bridge multilevel converter for grid-connected photovoltaic systems," *IEEE Trans. Ind. Electron.*, vol. 56, no. 11, pp. 4399–4406, Nov. 2009.

[13] J. Chavarria, D. Biel, F. Guinjoan, C. Meza, and J. Negroni, "Energy-balance control of PV cascaded multilevel grid-connected converters under level-shifted and phase-shifted PWMs," *IEEE Trans. Ind. Electron.*, vol. 60, no. 1, pp. 98–111, Jan. 2013.

[14] W. Zhao, H. Choi, G. Konstantinou, M. Ciobotaru, and V. Agelidis, "Cascaded H-bridge multilevel converter for large-scale PV grid-integration with isolated DC-DC stage," in *Proc. IEEE PEDG 2012*, pp. 849–856.

[15] L. Liu, H. Li, Y. Xue, and W. Liu, "Reactive power compensation and optimization strategy for grid-interactive cascaded photovoltaic systems," *IEEE Trans. Power Electron.*, vol. 30, no. 1, pp. 188–202, Jan. 2015.

[16] L. Liu, H. Li, Y. Xue, and W. Liu, "Decoupled active and reactive power control for large-scale grid-connected photovoltaic systems using cascaded modular multilevel converters, *IEEE Trans. Power Electron.*, vol. 30, no. 1, pp. 176–187, Jan. 2015.

[17] Y. Shi, R. Li, H. Li, and Y. Xue, "High-frequency-link based grid-tied PV system with small dc-link capacitor and low-frequency ripple-free maximum power point tracking," *IEEE Trans. Power Electron.*, vol. 31, no. 1, pp. 328–339, Jan. 2016.

[18] T. J. Summers, R. E. Betz, and G. Mirzaeva, "Phase leg voltage balancing of a cascaded H-Bridge converter based STATCOM using zero sequence injection," in *Proc. EPE 2009*, pp. 1–10.

[19] M. Coppola, F. D. Napoli, P. Guerriero, D. Iannuzzi, D. Daliento, A. D. Pizzo, "An FPGA-based advanced control strategy of a grid-tied PV CHB inverter," *IEEE Trans. Power Electron.*, vol. 31, no. 1, pp. 806–816, Jan. 2016.

[20] C. Townsend, T. Summers, and R. Betz, "Control and modulation scheme for a cascaded H-bridge multi-level converter in large scale photovoltaic systems," in *Proc. IEEE ECCE 2012*, pp. 3707–3714.

[21] Y. Yu, G. Konstantinou, B. Hredzak, and V. G. Agelidis, "Power balance of cascaded H-bridge multilevel converters for large-scale photovoltaic integration," *IEEE Trans. Power Electron.*, vol. 31, no. 1, pp. 292–303, Jan. 2016.

[22] S. Rivera, B. Wu, S. Kouro, and D. Zhang, "Cascaded H-bridge multilevel converter topology and three-phase balance control for large scale photovoltaic systems," in *Proc. IEEE PEDG 2012*, pp. 690–697.

[23] B. Xiao, L. Hang, J. Mei, C. Riley, L. Tolbert, and B. Ozpineci, "Modular cascaded H-bridge multilevel PV inverter with distributed MPPT for grid-connected applications," *IEEE Trans. Ind. Appl.*, vol. 51, no. 2, pp. 1722–1731, Mar.-Apr. 2015.

[24] Y. Yu, G. Konstantinou, B. Hredzak, and V. G. Agelidis, "Power balance optimization of cascaded H-bridge multilevel converters for large-scale photovoltaic integration," *IEEE Trans. Power Electron.*, vol. 31, no. 2, pp. 1108–1120, Feb. 2016.

[25] P. Sochor, and H. Akagi, "Theoretical comparison in energy-balancing capability between star- and delta-configured modular multilevel cascade inverters for utility-scale photovoltaic systems," *IEEE Trans. Power Electron.*, vol. 31, no. 3, pp. 1980–1992, Mar. 2016.

[26] Y. Yu, G. Konstantinou, B. Hredzak, and V. G. Agelidis, "On extending the energy balancing limit of multilevel cascaded H-bridge converters for large-scale photovoltaic farms," in *Proc. AUPEC 2013*, pp. 1–6.

[27] Y. Yu, G. Konstantinou, B. Hredzak, and V. G. Agelidis, "Optimal zero sequence injection in multilevel cascaded H-bridge converter under unbalanced photovoltaic power generation," in *Proc. IPEC 2014*, pp. 1458–1465.